Resolved target detection in clutter using correlated, dual-band imagery

Larry B. Stotts

Resolved target detection in clutter using correlated, dual-band imagery

Larry B. Stotts*
Science and Technology Associates, Resident Consultant, 4100 North Fairfax Drive, Suite 910, Arlington, Virginia 22203, United States

Abstract. This paper develops a log-likelihood ratio test statistic for resolved target detection in dual-band imagery because the previous work indicates that most of the processing gains come from processing just two bands. Simple, closed-form equations for the closed-form probabilities of false alarm and detection are given. A computer simulation validates the theory. A constant false alarm rate version of the theory is applied to real available multiband data with quasi-resolved target sets and fixed clutter noise. The results show very reasonable performance in target detectability using three sets of correlated dual-band images. Finally, this paper shows that the resolved target detection problem depends on the weighted difference between the dual-band target contrasts. The theoretical development reaffirms that the signal-to-noise ratio or contrast-to-noise ratio is approximately the weighted difference squared, divided by the normalized total image noise variance. © *The Authors. Published by SPIE under a Creative Commons Attribution 3.0 Unported License. Distribution or reproduction of this work in whole or in part requires full attribution of the original publication, including its DOI.* [DOI: 10.1117/1.OE.54.10.103109]

1 Introduction

One of the most challenging problems is detecting dim targets in complex optical images. Here, the term "dim" means low contrast. The classic method for determining the target's presence is to employ a spatially matched filter (MF) on the zero-mean image of interest and to compare positive and negative exceedances to a threshold. As expected, the filter is designed for a specific target profile and a statistically known background clutter. In digital imagery, the signal-to-noise ratio (SNR) gain from this procedure is equal to the number of independent samples composing the profile of the target. Unfortunately, this may not be enough gain to trigger the detection of a target while minimizing false detections if the target is dim.

Several researchers expanded the processing degrees of freedom from just spatial processing to spatial and temporal processing[1–3] and spatial and hyperspectral processing.[4–20] The goal here is to minimize the background clutter and maximize the detectability of any targets in the imagery. All of these papers exploited the classical theory of additive signal detection where the two possible hypotheses are signal (s)-plus-noise and noise alone. Schaum and Daniel recently complained about the continued use of the additive model in electro-optical image analysis because of its "phenomenological inaccuracy."[18] They advocated the use of the more appropriate replacement target model. Their proposed solution was to apply continuum fusion methodology[18–20] to multispectral imagery, and they presented a detailed paper on its application, with examples to validate their approach to replacement model detection analysis.[18] As pointed out by Goudail in a private communication, other researchers have been developing techniques for the replacement target model

for some time under the topic of pattern recognition with nonoverlapping targets and background clutter.[21] The overarching approach taken by all of these researchers was to make it an estimation and detection problem rather than trying to tackle the classical approach.[20]

The paper investigates resolved target detection hypothesis testing using highly correlated two-color imagery to obtain large signal processing gains to reduce clutter and extract the target's location if it is present. It extends the classical approach development of Stotts and Hoff[21] to dual-band target detection. This approach assumes that the target profile is contained in a fixed number of pixels since many applications use detection as the first step to classification and identification of the target,[22–31] namely, MF detection (leakage of background clutter into edge pixels reduces the maximum filter gain but usually not by a large amount because of the potentially large number of pixels a resolved image contains[1–3]). The reason for only looking at two bands is that many previous research papers have found that "additive noise" detector performances with real data are lower as we spread the processing gain across many bands, which will be discussed in the next section. This also should be true for replacement model theories. This motivated the author to focus on the dual spectral replacement problem where the two bands are correlated enough to reduce the background clutter noise down to the system noise level, hopefully leaving some residual target signatures intact after algorithmic processing. The resulting approach provided simple expressions for the test statistic and the probabilities of false alarm and detection, unlike the normal quadratic detector that requires very complicated computation of these last two entities, even using either Monte Carlo simulations[10,31] or numerical methods.[32] Finally, this approach reconfirms that the electrical SNR is related to the Weber contrast[33] and the normalized noise variance, as shown by Stott and Hoff.[21]

---

*Address all correspondence to: Larry B. Stotts, E-mail: lbstotts@gmail.com

2 Background and Motivation for Two-Band Only Optical Detection Strategy

In the majority of the optical target detection strategies in multiband imagery, the solution involves the likelihood ratio, and the required resolved/unresolved target and noise intensity distributions obey multivariate Gaussian probability density functions (PDFs) of the form

$$H_0: \boldsymbol{x} \sim N(\bar{\boldsymbol{j}_n}, \boldsymbol{R}_n) \tag{1}$$

and

$$H_1: \boldsymbol{x} \sim N(\bar{\boldsymbol{j}_n}, \boldsymbol{R}_t), \tag{2}$$

where $\bar{\boldsymbol{j}_n}$ and $\boldsymbol{R}_n$ and $\bar{\boldsymbol{j}_t}$ and $\boldsymbol{R}_t$ represent the mean vector and covariance matrices for hypotheses H_k, $k = 0, 1$, respectively. Depending on the problem addressed, $\bar{\boldsymbol{j}}_n$ and $\bar{\boldsymbol{j}}_t$ can contain more than the background and target means, respectively, and their covariance matrices $\boldsymbol{R}_n$ and $\boldsymbol{R}_t$ can have correlated and uncorrelated data. At a minimum, we know that both distributions will contain some sort of system noise that depends on the optical sensor design.

In the general case where $\boldsymbol{R}_n \neq \boldsymbol{R}_t$, the likelihood ratio is given by

$$\Lambda(\boldsymbol{x}) = \frac{|\boldsymbol{R}_n|^{1/2} \exp[-(\boldsymbol{x}-\boldsymbol{j}_t)^T \boldsymbol{R}_t^{-1}(\boldsymbol{x}-\boldsymbol{j}_t)]}{|\boldsymbol{R}_t|^{1/2} \exp[-(\boldsymbol{x}-\boldsymbol{j}_n)^T \boldsymbol{R}_n^{-1}(\boldsymbol{x}-\boldsymbol{j}_n)]} \begin{matrix} > \Lambda_0; \text{to choose } H_1 \\ \leq \Lambda_0; \text{to choose } H_0 \end{matrix}. \tag{3}$$

Taking the logarithm and manipulating terms, we obtain the following detection statistic:

$$\begin{aligned} y = D(\boldsymbol{x}) &= (\boldsymbol{x}-\boldsymbol{j}_n)^T \boldsymbol{R}_n^{-1}(\boldsymbol{x}-\boldsymbol{j}_n) \\ &- (\boldsymbol{x}-\boldsymbol{j}_t)^T \boldsymbol{R}_t^{-1}(\boldsymbol{x}-\boldsymbol{j}_t) \quad \begin{matrix} > g_0; \text{to choose } H_1 \\ \leq g_0; \text{to choose } H_0 \end{matrix}, \end{aligned} \tag{4}$$

which compares the Mahalanobis distance of the spectrum under test from the means of the background and target PDFs.[10] In the above, g_0 is the resulting threshold after the term adjustment. Equation (4) is known as the quadratic detector.

Manolakis et al. noted that the variable $y = D$ is a random variable whose probability density depends on which hypothesis is true.[10] If the two conditional probability densities, $f(q|H_1)$ and $f(q|H_0)$, are known, then the probabilities of detection and false alarm are given by

$$Q_d = \int_{g_0}^{\infty} f(q|H_1) \mathrm{d}q, \tag{5}$$

and

$$Q_{fa} = \int_{g_0}^{\infty} f(q|H_0) \mathrm{d}q. \tag{6}$$

They also note that the computation of these two integrals is quite complicated, and the receiver operating characteristic (ROC) curves can only be evaluated, not so simply, by using Monte Carlo simulation[31] or numerical techniques.[32]

Another approach to the above is the Reed–Xiaoli (RX) algorithm that provides a generalized likelihood ratio test (GLRT) approach to finding targets in clutter.[34–37,17] Specifically, it is a generalized hypothesis test formulated by partitioning the received bands into two groups. In one group, targets exhibit substantial coloring in their signatures but either behave like gray bodies or emit negligible radiant energy in the other group. Xu et al. developed the following adaptive decision statistics:[36]

$$g(\boldsymbol{J}) = \frac{(\boldsymbol{b}_s^T \boldsymbol{R}^{-1} \boldsymbol{J} \boldsymbol{s})^2}{(\boldsymbol{b}_s^T \boldsymbol{R}^{-1} \boldsymbol{b}_s)(1 - \frac{1}{N}\boldsymbol{J}^T \boldsymbol{R}^{-1} \boldsymbol{J} \boldsymbol{s})} \geq g_0, \tag{7}$$

with

$$g_0 = K / \left(\frac{1}{r_0} - 1\right) \tag{8}$$

[see Ref. 36]. In the above, the multispectral sensor is assumed to create a set of $\boldsymbol{J}$-pixel correlated measurement vectors for the M band. The resulting $M \times K$ matrix is given by

$$\boldsymbol{J} = [\boldsymbol{j}(1), \boldsymbol{j}(2), \ldots, \boldsymbol{j}(K)], \tag{9}$$

which represents K independent pixel observations from M correlated image scenes taken from a local window size of $L_x \times L_y = K$, where the clutter is considered stationary. Their measurement vectors of spectral observations in each pixel are given as

$$\boldsymbol{j}(\boldsymbol{k}) = [j_1(k), j_2(k), \ldots, j_M(k)]^T, \tag{10}$$

for $\{k = 1, 2, \ldots, K\}$. Their approach assumes a known target signal to be characterized by two vectors:

$$\boldsymbol{b} = [b_1, b_2, \ldots, b_M]^T, \tag{11}$$

and

$$\boldsymbol{s} = [s_1, s_2, \ldots, s_K]^T, \tag{12}$$

where

$$\boldsymbol{b}_s = \boldsymbol{b} / \|\boldsymbol{b}\|, \tag{13}$$

and

$$\boldsymbol{s}^T \boldsymbol{s} = \|\boldsymbol{s}\|^2 = 1. \tag{14}$$

Figures 1(a) and 1(b) show the probability of detection versus generalized SNR for $Q_{fa} = 10^{-5}$ for $K = 49$ and $K = 81$, respectively, as a function of the number of bands M. Figures 2(a) and 2(b) show the probability of detection versus GSNR for $Q_{fa} = 10^{-5}$ for $M = 2$ and $M = 6$, respectively, as a function of pixel observations K. In these figures, GSNR is the GSNR defined by the equation

$$\text{GSNR} \equiv \boldsymbol{b}_s^T \boldsymbol{R}^{-1} \boldsymbol{b}_s \|\boldsymbol{s}\|^2. \tag{15}$$

The constant false alarm rate (CFAR) probability of the detection curve for a perfect MF and $Q_{fa} = 10^{-5}$ is included in these two figures to better illustrate the effects of the numbers of pixel observations and bands, K and M, on Q_d.[36] It is clear in Figs. 1 and 2 that for a given number of bands M, the probability of a false alarm and the CFAR probability of detection both improve as the number of pixel observations increases. The limit is when K goes to infinity, which results in the
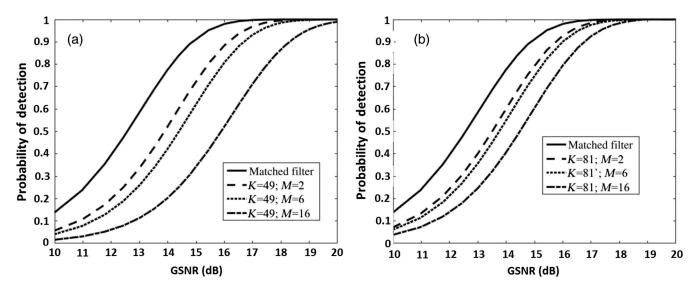
Fig. 1 CFAR probability of detection versus generalized signal-to-noise ratio (GSNR) for (a) $K = 49$ and (b) $K = 81$, as a function of spectral bands M, as compared to that of a perfect matched filter (MF).
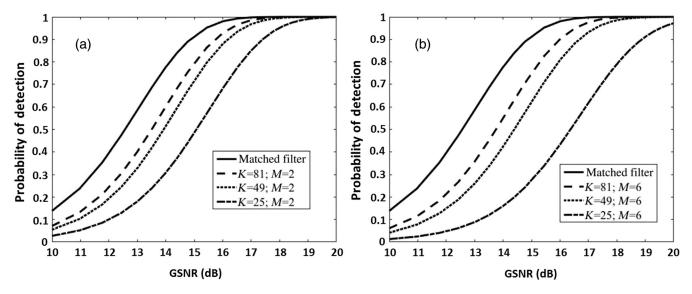

Fig. 2 CFAR probability of detection versus GSNR for (a) $M = 2$ and (b) $M = 6$, as a function of pixel observations K, as compared to that of a perfect matched filter.

perfect MF curves these two graphs.[36] On the other hand, the CFAR probability of detection for a fixed number of pixel observations decreases if more bands are used to provide the same GSNR. This is because the number of unknown parameters in the covariance matrix R increases as M gets larger.[36]

Hoff et al.[6,7] extended to multiple bands the two-band weighted difference (additive noise) hypothesis test developed by Stotts.[2] Figures 3 and 4 show the output SNR of their generalized weighted spectral difference detector using thermal infrared multispectral scanner (TIMS) and spatially modulated, imaging, Fourier transform interferometer spectrometer (SMIFTS) image sets, respectively.[6,7] The first figure indicates that more than 20 dB gain was obtained for detection by processing beyond one spectral band. There was a significant gain of 16 dB in processing just two spectral bands. Since the first two images processed are very highly

correlated, two-band processing appears to cancels most of the image clutter. This figure shows that processing an additional spectral image will not reduce the clutter variance significantly over that of the dual-band processing. (The curves also indicate that the output SNR will gradually level off if more target-reference bands are added.) The second figure confirms these comments using a different dataset. Xu et al.[36] and Hallenborg et al.[17] also applied a form of the RX algorithm to TIMS data and found similar performance, that is, most performance occurs in fewer bands with a small increase in SNR with additional bands.

Results like these suggest that highly correlated, dual-band images provide close to the maximum signal processing gain possible. In the author's opinion, adding target and clutter bands gives marginal increased detector performance given the increased computational and sensor design complexity that is required. As we are interested in large signal
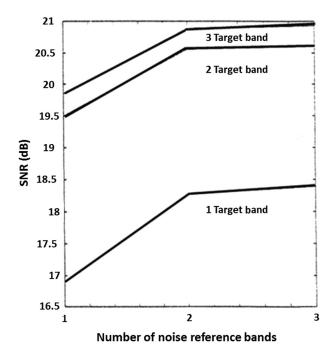
Fig. 3 Incremental improvement in signal-to-noise ratio (SNR) provided by adding clutter and target reference bands collected by thermal infrared multispectral scanner (TIMS).[38]
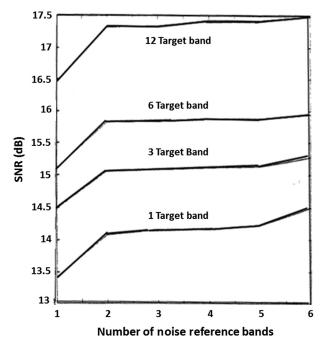

Fig. 4 The incremental improvement in SNR provided by adding clutter and target reference bands collected by SMIFTS.[38]

processing gains with the least complexity, the remainder of the paper will deal with the two-band optical detection problem.

3 Dual-Band Resolved Target Detection Theory

Let us assume hypothesis H_0 is where we have background clutter plus system noise only in the two images and within the N pixel template. The resulting vector is given by

$$j_n = \begin{bmatrix} i_1 - b_1 - n_1 \\ i_2 - b_2 - n_2 \end{bmatrix}, \tag{16}$$

where i_1 and i_2 are the image vectors; b_1 and b_2 are the correlated background clutter vectors (i.e., fixed background structure from trees, grass, roads, etc.) at wavelengths λ_1 and λ_2, respectively, contained in images i_1 and i_2; and n_1; and n_2 are the mean image vectors for the system noise contained in images i_1 and i_2, respectively.

The covariance matrix for hypothesis H_0 is given by

$$R_n = \{j_n j_n^T\}, \tag{17}$$

$$= \begin{pmatrix} \sigma_1^2 I & p_{12} I \\ p_{21} I & \sigma_2^2 I \end{pmatrix}, \tag{18}$$

with

$$\sigma_n^2 \equiv \text{statistical variance of image } i_n \text{ under } H_0$$
$$= \sigma_{b1}^2 + \sigma_{sn}^2 \approx \sigma_{n1}^2, \tag{19}$$

$$\sigma_t^2 \equiv \text{statistical variance of image } i_t \text{ under } H_0$$
$$= \sigma_{b2}^2 + \sigma_{sn}^2 \approx \sigma_{b2}^2, \tag{20}$$

$$\sigma_t^2 \equiv \text{statistical variance of system noise}$$

because one does not see a salt-and-pepper speckle of system noise in good-quality imagery. In Eq. (18), we have

$$p_{12} = E\{i_1 i_2^T\} = \sigma_{b1} \sigma_{b2} \rho = p_{21}. \tag{21}$$

In this development, the image background clutter is assumed to be correlated, and the system noise is assumed to be uncorrelated.

The inverse matrix R_n^{-1} can easily be shown to equal

$$R_n^{-1} = \begin{pmatrix} \sigma_f^2 I & p I \\ p I & \sigma_g^2 I \end{pmatrix}, \tag{22}$$

where

$$\sigma_f^2 = \frac{1}{\sigma_{b1}^2 (1 - \rho^2)}, \tag{23}$$

$$\sigma_g^2 = \frac{1}{\sigma_{b2}^2 (1 - \rho^2)}, \tag{24}$$

$$p = \frac{-\rho}{\sigma_{b1} \sigma_{b2} (1 - \rho^2)}, \tag{25}$$

and ρ is the correlation coefficient between the two images.

Similarly, we find for hypothesis H_1 that its resulting vector is given by

$$j_t = \begin{bmatrix} i_1 - s_1 - n_1 \\ i_2 - s_2 - n_2 \end{bmatrix}, \tag{26}$$

where s_1 and s_2 are the image vectors for our target pixels sampled at wavelengths λ_1 and λ_2, respectively, contained in

images i_1 and i_2. The covariance matrix for hypothesis H_1 is equal to

$$\boldsymbol{R}_t = \varepsilon\{\boldsymbol{j}\boldsymbol{j}_1^T\}, \tag{27}$$

$$= \sigma_{sn}^2 \begin{bmatrix} \boldsymbol{I} & 0 \\ 0 & \boldsymbol{I} \end{bmatrix}. \tag{28}$$

This implies that

$$\boldsymbol{R}_t^{-1} = \sigma_{sn}^{-2} \begin{bmatrix} \boldsymbol{I} & 0 \\ 0 & \boldsymbol{I} \end{bmatrix}, \tag{29}$$

where $\boldsymbol{I}$ and 0 are the $N \times N$ identity and null matrices, respectively.

Let us remove the signal and system noise-mean image vectors from both images. Then the resulting vector for H_0 becomes

$$\boldsymbol{m}_n = \begin{bmatrix} \boldsymbol{i}_1 - \boldsymbol{b}_1 + \boldsymbol{s}_1 \\ \boldsymbol{i}_2 - \boldsymbol{b}_2 + \boldsymbol{s}_2 \end{bmatrix}, \tag{30}$$

$$= \begin{bmatrix} \boldsymbol{i}_1 + \boldsymbol{b}_1 \boldsymbol{C}_1 \\ \boldsymbol{i}_2 + \boldsymbol{b}_2 \boldsymbol{C}_2 \end{bmatrix}, \tag{31}$$

where

$$\boldsymbol{C}_k = \frac{\boldsymbol{s}_k - \boldsymbol{b}_k}{\boldsymbol{b}_k}, \text{ for k } = 1, 2 \tag{32}$$

is the Weber contrast column vector for image $\boldsymbol{m}_0$.

The resulting vector for hypothesis H_1 is given by

$$\boldsymbol{m}_t = \begin{bmatrix} \boldsymbol{i}_1 \\ \boldsymbol{i}_2 \end{bmatrix}, \tag{33}$$

and its associated covariance matrix for $\boldsymbol{m}_0$ is still $\boldsymbol{R}_t^{-1}$. Substituting into Eq. (4), we have

$$
\begin{aligned}
\ln \Lambda &= \ln \left[\frac{p_1(i_2)}{p_0(i_0)} \right] \\
&= \ln \left[\frac{|\boldsymbol{R}_n|^{1/2}}{|\boldsymbol{R}_t|^{1/2}} \right] - \sigma_{sn}^{-2} [\boldsymbol{i}_1 \ \boldsymbol{i}_2] \begin{bmatrix} \boldsymbol{I} & 0 \\ 0 & \boldsymbol{I} \end{bmatrix} \begin{bmatrix} \boldsymbol{i}_1 \\ \boldsymbol{i}_2 \end{bmatrix} \\
&\quad + [\boldsymbol{i}_1 + \boldsymbol{b}_1\boldsymbol{C}_1 \ \boldsymbol{i}_2 + \boldsymbol{b}_2\boldsymbol{C}_2] \begin{pmatrix} \sigma_f^2 \boldsymbol{I} & p\boldsymbol{I} \\ p\boldsymbol{I} & \sigma_g^2\boldsymbol{I} \end{pmatrix} \begin{bmatrix} \boldsymbol{i}_1 + \boldsymbol{b}_1\boldsymbol{C}_1 \\ \boldsymbol{i}_2 + \boldsymbol{b}_2\boldsymbol{C}_2 \end{bmatrix}, \\
&= \ln \left[\frac{|\boldsymbol{R}_0|^{1/2}}{|\boldsymbol{R}_1|^{1/2}} \right] - \left[\frac{\sigma_3^2}{\sigma_{sn}^2 \sigma_{b1}^2 (1-\rho^2)} \right] \boldsymbol{i}_1^T \boldsymbol{i}_1 \\
&\quad - \left[\frac{\sigma_4^2}{\sigma_{sn}^2 \sigma_{b2}^2 (1-\rho^2)} \right] \boldsymbol{i}_2^T \boldsymbol{i}_2 + \frac{(\boldsymbol{i}_1^T\boldsymbol{b}_1\boldsymbol{C}_1 + \boldsymbol{b}_1^T\boldsymbol{C}_1^T\boldsymbol{i}_1 + \boldsymbol{b}_1^T\boldsymbol{C}_1^T\boldsymbol{b}_1\boldsymbol{C}_1)}{\sigma_{b1}^2 (1-\rho^2)} \\
&\quad - \rho \frac{(\boldsymbol{i}_2 + \boldsymbol{b}_2\boldsymbol{C}_2)^T(\boldsymbol{i}_1 + \boldsymbol{b}_1\boldsymbol{C}_1)}{\sigma_{b1}\sigma_{b2}(1-\rho^2)} - \rho \frac{(\boldsymbol{i}_1 + \boldsymbol{b}_1\boldsymbol{C}_1)^T(\boldsymbol{i}_2 + \boldsymbol{b}_2\boldsymbol{C}_2)}{\sigma_{b1}\sigma_{b2}(1-\rho^2)} \\
&\quad + \frac{(\boldsymbol{i}_2^T\boldsymbol{b}_2\boldsymbol{C}_2 + \boldsymbol{b}_2^T\boldsymbol{C}_2^T\boldsymbol{i}_2 + \boldsymbol{b}_2^T\boldsymbol{C}_2^T\boldsymbol{b}_2\boldsymbol{C}_2)}{\sigma_{b2}^2(1-\rho^2)} \begin{array}{l} > \ln\Lambda_0; \text{to choose } H_1 \\ \leq \ln\Lambda_0; \text{to choose } H_0 \end{array},
\end{aligned} \tag{34}
$$

where

$$\sigma_3^2 = \sigma_{b1}^2(1-\rho^2) - \sigma_{sn}^2, \tag{35}$$

and

$$\sigma_4^2 = \sigma_{b2}^2(1-\rho^2) - \sigma_{sn}^2. \tag{36}$$

Rewriting Eq. (34), we have

$$
\begin{aligned}
g &= \left[\boldsymbol{i}_1^T\boldsymbol{i}_1 + \left(\frac{\sigma_{b1}^2}{\sigma_{b2}^2} \right)\boldsymbol{i}_2^T\boldsymbol{i}_2 + (\boldsymbol{i}_1^T\boldsymbol{b}_1\boldsymbol{C}_1 + \boldsymbol{b}_1^T\boldsymbol{C}_1^T\boldsymbol{i}_1 + \boldsymbol{b}_1^T\boldsymbol{C}_1^T\boldsymbol{b}_1\boldsymbol{C}_1) \right. \\
&\quad - \rho\left(\frac{\sigma_{b1}}{\sigma_{b2}} \right)(\boldsymbol{i}_2^T\boldsymbol{i}_1 + \boldsymbol{i}_2^T\boldsymbol{b}_1\boldsymbol{C}_1 + \boldsymbol{b}_2^T\boldsymbol{C}_2^T\boldsymbol{i}_1 + \boldsymbol{b}_2^T\boldsymbol{C}_2^T\boldsymbol{b}_1\boldsymbol{C}_1) \\
&\quad - \rho\left(\frac{\sigma_{b1}}{\sigma_{b2}} \right)(\boldsymbol{i}_1^T\boldsymbol{i}_2 + \boldsymbol{i}_1^T\boldsymbol{b}_2\boldsymbol{C}_2 + \boldsymbol{b}_1^T\boldsymbol{C}_1^T\boldsymbol{i}_2 + \boldsymbol{b}_1^T\boldsymbol{C}_1^T\boldsymbol{b}_2\boldsymbol{C}_2) \\
&\quad + \left(\frac{\sigma_{b1}^2}{\sigma_{b2}^2} \right)(\boldsymbol{i}_2^T\boldsymbol{b}_2\boldsymbol{C}_2 + \boldsymbol{b}_2^T\boldsymbol{C}_2^T\boldsymbol{i}_2 \\
&\quad \left. + \boldsymbol{b}_2^T\boldsymbol{C}_2^T\boldsymbol{b}_2\boldsymbol{C}_2) \right] \begin{array}{l} > g_0; \text{to choose } H_1 \\ \leq g_0; \text{to choose } H_0 \end{array}.
\end{aligned} \tag{37}
$$

Since we assume that $\sigma_{bi}^2(1-\rho^2) \ll \sigma_{sn}^2$ for $i = 1, 2$. Here,

$$g_0 = \sigma_{b1}^2(1-\rho^2)\left\{ \ln\Lambda_0 - \ln\left[\frac{p_1(i_2)}{p_0(i_0)} \right] \right\}. \tag{38}$$

In Eq. (38), we adjust $\ln\Lambda_0$ to keep g_0 nonzero for correlation coefficients close to 1. This last assumption $\sigma_{bi}^2(1-\rho^2) \ll \sigma_{sn}^2$ says that the best weighted difference noise reduction essentially is where we become system noise–limited and the residual clutter is negligible. This condition would be expected for the closely spaced bands.[39,4,6,7,17]

If we further assume that $\rho^2 \cong 1$, with the appropriate adjustments of $\ln\Lambda_0$ to keep g_0 nonzero, then Eq. (37) becomes

$$
\begin{aligned}
g &= \left[\boldsymbol{i}_1^T\boldsymbol{i}_1 + \left(\frac{\sigma_{b1}^2}{\sigma_{b2}^2} \right)\boldsymbol{i}_2^T\boldsymbol{i}_2 + (\boldsymbol{i}_1^T\boldsymbol{b}_1\boldsymbol{C}_1 + \boldsymbol{b}_1^T\boldsymbol{C}_1^T\boldsymbol{i}_1 + \boldsymbol{b}_1^T\boldsymbol{C}_1^T\boldsymbol{b}_1\boldsymbol{C}_1) \right. \\
&\quad - \rho\left(\frac{\sigma_{b1}}{\sigma_{b2}} \right)(\boldsymbol{i}_2^T\boldsymbol{i}_1 + \boldsymbol{i}_2^T\boldsymbol{b}_1\boldsymbol{C}_1 + \boldsymbol{b}_2^T\boldsymbol{C}_2^T\boldsymbol{i}_1 + \boldsymbol{b}_2^T\boldsymbol{C}_2^T\boldsymbol{b}_1\boldsymbol{C}_1) \\
&\quad - \rho\left(\frac{\sigma_{b1}}{\sigma_{b2}} \right)(\boldsymbol{i}_1^T\boldsymbol{i}_2 + \boldsymbol{i}_1^T\boldsymbol{b}_2\boldsymbol{C}_2 + \boldsymbol{b}_1^T\boldsymbol{C}_1^T\boldsymbol{i}_2 + \boldsymbol{b}_1^T\boldsymbol{C}_1^T\boldsymbol{b}_2\boldsymbol{C}_2) \\
&\quad + \left(\frac{\sigma_{b1}^2}{\sigma_{b2}^2} \right)\rho^2(\boldsymbol{i}_2^T\boldsymbol{b}_2\boldsymbol{C}_2 + \boldsymbol{b}_2^T\boldsymbol{C}_2^T\boldsymbol{i}_2 \\
&\quad \left. + \boldsymbol{b}_2^T\boldsymbol{C}_2^T\boldsymbol{b}_2\boldsymbol{C}_2) \right] \begin{array}{l} > g_0; \text{to choose } H_1 \\ \leq g_0; \text{to choose } H_0 \end{array}
\end{aligned} \tag{39}
$$

$$
= \left| \left| \left[\boldsymbol{i}_1 - \rho\left(\frac{\sigma_{b1}}{\sigma_{b2}} \right)\boldsymbol{i}_2 \right] \right. \right. \\
\left. \left. + \left[\boldsymbol{b}_1\boldsymbol{C}_1 - \rho\left(\frac{\sigma_{b1}}{\sigma_{b2}} \right)\boldsymbol{b}_2\boldsymbol{C}_2 \right] \right| \right|^2 \begin{array}{l} > g_0; \text{to choose } H_1 \\ \leq g_0; \text{to choose } H_0 \end{array}. \tag{40}
$$

Normalizing Eq. (40), we obtain the following test statistic:

$$\frac{1}{N}\left|\left[\boldsymbol{i}_1 - \rho\left(\frac{\sigma_{b_1}}{\sigma_{b2}}\right)\boldsymbol{i}_2\right] + \left[\boldsymbol{b}_1\boldsymbol{C}_1 - \rho\left(\frac{\sigma_{b1}}{\sigma_{b2}}\right)\boldsymbol{b}_2\boldsymbol{C}_2\right]\right|^2 \begin{array}{c} > \text{G}_0 \\ \le \text{G}_0 \end{array}.$$

(41)

The $[\boldsymbol{i}_1 - \rho(\sigma_{b1}/\sigma_{b2})\boldsymbol{i}_2]$ term in Eq. (41) is analogous to the processing for the side-lobe canceller radar, that is, the weighted-difference equation.[40,41] It can be shown that the weight $\rho(\sigma_1/\sigma_2)$ minimizes the difference-image variance in a least-mean-square error sense.[41]

Equation (40) has the form of the equation

$$\frac{1}{N}\sum_{n=1}^{N}|x_n + A_n|^2,$$

(42)

which implies that the PDF for our test statistics is the (normalized) central chi-squared density functions with N degrees of freedom of the form

$$f(\nu)d\nu \equiv \frac{N}{2}\left(\frac{N\nu}{\lambda}\right)^{(N-2)/4}e^{[-(\lambda+N\nu)/2]}\boldsymbol{I}_{\frac{N-2}{2}}(\sqrt{\lambda N\nu})d\nu,$$

(43)

$$= f_\chi(\nu; N, \lambda)d\nu,$$

(44)

with

$$\vartheta = \sum_{n=1}^{N}A_n^2/\sigma^2.$$

(45)

In Ref. 21, the quantity $\vartheta \ge 0$ is called the noncentrality parameter. Consequently, the probabilities of false alarm and detection are given by

$$Q_{fa} = \int_{G_0}^{\infty}f_\chi(\nu; N, \vartheta_0)dq,$$

(46)

and

$$Q_d = \int_{G_0}^{\infty}f_\chi(\nu; N, \vartheta_1)dq,$$

(47)

respectively, where

$$\vartheta_0 = \sum_{n=1}^{N}A_n^2(H_0)/\sigma_T^2 = \frac{\left|\boldsymbol{b}_1\boldsymbol{C}_1 - \rho\left(\frac{\sigma_1}{\sigma_2}\right)\boldsymbol{b}_2\boldsymbol{C}_2\right|^2}{\sigma_T^2},$$

(48)

$$\vartheta_1 = 4\vartheta_0,$$

(49)

with

$$\sigma^2 = \sigma_1^2(1-\rho^2) + \alpha\sigma_{sn}^2.$$

(50)

The $\alpha = [1 + \rho(\sigma_1/\sigma_2)]$ multiplier on the system noise variance in Eq. (50) comes from the increased variance produced by the weighted difference of the two images.

Following Ref. 21, we define the difference to be the contrast noise ratio (CNR), or

$$\text{CNR} = \vartheta_1 - \vartheta_0$$

$$= \frac{4\left|\left[\boldsymbol{b}_1\boldsymbol{C}_1 - \rho\left(\frac{\sigma_{b1}}{\sigma_{b2}}\right)\boldsymbol{b}_2\boldsymbol{C}_2\right]\right|^2}{(\alpha\sigma_{sn}^2)} - \frac{\left|\left[\boldsymbol{b}_1\boldsymbol{C}_1 - \rho\left(\frac{\sigma_{b1}}{\sigma_{b2}}\right)\boldsymbol{b}_2\boldsymbol{C}_2\right]\right|^2}{[\sigma_{b1}^2(1-\rho^2) + \alpha\sigma_{sn}^2]}$$

$$\approx \frac{4\left|\left[\boldsymbol{b}_1\boldsymbol{C}_1 - \rho\left(\frac{\sigma_{b1}}{\sigma_{b2}}\right)\boldsymbol{b}_2\boldsymbol{C}_2\right]\right|^2}{[\sigma_{b1}^2(1-\rho^2) + \alpha\sigma_{sn}^2]} - \frac{\left|\left[\boldsymbol{b}_1\boldsymbol{C}_1 - \rho\left(\frac{\sigma_{b1}}{\sigma_{b2}}\right)\boldsymbol{b}_2\boldsymbol{C}_2\right]\right|^2}{[\sigma_{b1}^2(1-\rho^2) + \alpha\sigma_{sn}^2]}.$$

(51)

$$= \frac{3\left|\left[\boldsymbol{b}_1\boldsymbol{C}_1 - \rho\left(\frac{\sigma_{b1}}{\sigma_{b2}}\right)\boldsymbol{b}_2\boldsymbol{C}_2\right]\right|^2}{[\sigma_{b1}^2(1-\rho^2) + \alpha\sigma_{sn}^2]}.$$
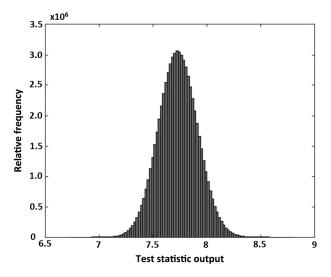
(52)

For constant contrast across the target areas, Eq. (52) becomes

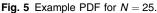$$\text{CNR} = \left\{\frac{NC_1^2}{\left[\frac{(\sigma_{b1}^2(1-\rho^2)+\alpha\sigma_t^2)}{b_1^2}\right]}\right\}\left[1 - \rho\left(\frac{\sigma_{b1}}{\sigma_{b2}}\right)\left(\frac{b_2C_2}{b_1C_1}\right)\right]^2.$$

(53)

Once again, we see that CNR depends on the Weber contrast squared, divided by the normalized variance, as found in the single channel case.[21] The ratio (b_2C_2/b_1C_1) is the color ratio between the two images. The $[\ldots]^2$ term in Eq. (53) always is positive no matter what the value of the color ratio is.

4 Theory Validations from Computer Simulation Results

Let us now determine if our false alarm and detection probabilities agree with computer simulation results. We begin by validating the equation for the probability of a false alarm. Specifically, we begin by creating two sets of correlated 8192×8192 Gaussian noise images with image correlation $\rho = 0.9995$ and image variances equal to $\sigma_{b1}^2 = 1.5$ and $\sigma_{b2}^2 = 1.0$, respectively. We then add separate, independent system noise with a zero mean and $\sigma_{sn}^2 = 0.01$ to each image. For these numbers, the weighted difference variance is equal to $\sigma_{WD}^2 = \sigma_{b1}^2(1-\rho^2)$, which is about a factor of 7 less than σ_t^2. For this simulation, we set the signal levels for the target in images 1 and 2 as 6 and 1, respectively, for all values of index n. Similarly, we set the background mean levels in images 1 and 2 as 2 and 1, respectively, for all values of index n. This means the pixel contrasts in images 1 and image 1 are 2 and 1, respectively. The next step was to process the two 8192×8192 image sets using the formula in Eq. (41) to create an estimated PDF for four MF sizes: $N = 25$, 49, 81, and 121. Figure 5 is one realization of the PDF from the $N = 25$ computer simulation. We next calculated its cumulative probability distribution against certain detection thresholds, then subtracted this result from unity so we could compare these results to our equation for the probability of a false alarm. Referring to Fig. 5, the value of $N = 25$ appears to be large enough that the PDF approximates a Gaussian PDF by the central limit theorem, which appears to be also true for the other values of N employed. As a result, we will use the Gaussian approximation of the noncentral chi-squared distribution in the calculations to come. From previous work,[21] we know that the probability of a false alarm for our problem may be approximated as

Fig. 5 Example PDF for $N = 25$.

$$Q_{fa} \approx \int_{G_0}^{\infty} \left(\frac{1}{\sqrt{2\pi s_0^2}} \right) e^{-(s-m_0)^2/s_0^2} ds, \quad (54)$$

with

$$m_0 = \frac{\sigma_T^2[\vartheta_0 + N]}{N}, \quad (55)$$

$$s_0^2 = \frac{\sigma_T^4[4\vartheta_0 + 2N]}{N^2}, \quad (56)$$

$$\vartheta_0 = \sum_{n=1}^{N} A_n^2(H_0)/\sigma_T^2 = \frac{\left| b_1 C_1 - \rho\left(\frac{\sigma_1}{\sigma_2}\right) b_2 C_2 \right|^2}{\sigma_T^2}, \quad (57)$$

and

$$\sigma_T^2 = \sigma_{b1}^2(1 - \rho^2) + \alpha\sigma_{sn}^2, \quad (58)$$

for large values of N. Figure 6 is a comparison of the computer simulation results and the probability of a false alarm using Eq. (54) as a function of the threshold for $N = 25, 49, 81,$ and 121 with image correlation $\rho = 0.9995$. This figure shows good agreement between theory and simulation, with the approximation getting better for low probabilities of a false alarm as N increases.

Similarly, we find that the probability of detection can be approximated as

$$Q_d \approx \int_{G_0}^{\infty} \left(\frac{1}{\sqrt{2\pi s_1^2}} \right) e^{-(s-m_1)^2/s_1^2} ds, \quad (59)$$

with

$$m_1 = \frac{\sigma_d^2[\vartheta_1 + N]}{N}, \quad (60)$$

$$s_1^2 = \frac{\sigma_d^4[\vartheta_1 + 2N]}{N^2}, \quad (61)$$

$$\vartheta_1 = 4\sum_{n=1}^{N} A_n^2(H_0)/\sigma_d^2, \quad (62)$$

and

$$\sigma_d^2 \approx \alpha\sigma_{sn}^2, \quad (63)$$

for large values of N. Figure 7 compares computer simulation results with the probability of detection using Eq. (59) as a function of the threshold for $N = 25, 49, 81,$ and 121. This figure again shows good agreement between theory and simulation. The probability of detection depicts the same kind of cross-over performance shown in the single-channel case reported by Stotts and Hoff.[21] As with the single-channel case, the computer simulation results verify the fact that this theory is valid when the weighted difference of the two image contrasts is negative.
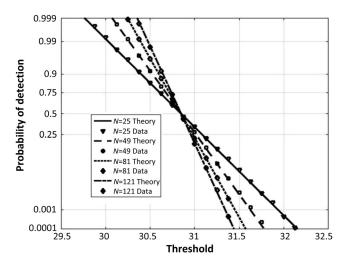

Fig. 6 Comparison of computer simulation results with probability of false alarm, Eq. (54), for $N = 25, 49, 81,$ and 121.

Fig. 7 Comparison of computer simulation results with probability of detection, Eq. (54), for $N = 25, 49, 81,$ and 121.
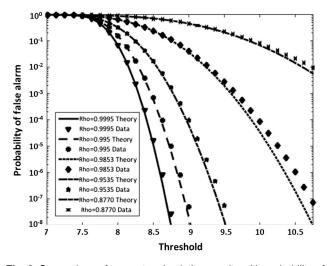
Fig. 8 Comparison of computer simulation results with probability of false alarm, Eq. (52), for $N = 25$ and $\rho = 0.9995$, 0.995, 0.9853, 0.9535, and 0.8771.

5 Assumptions Sensitivity

Recall in the previous section that our test statistic development required $\sigma_{bi}^2 \gg \sigma_{sn}^2$ and $\sigma_{bi}^2(1 - \rho^2) \ll \sigma_{sn}^2$ for $i = 1, 2$. As noted earlier, the former assumption is not a constraint because all good-quality images do not have any system noise speckle evident. However, the second assumption is not as clear. To assess the effect of this assumption, a set of similar computer simulations as described above were performed, but the value of N was kept fixed and the image correlation coefficients were varied. Figures 8–10 shows a comparison of computer simulation results and the probability of a false alarm using Eq. (54) as a function of the threshold for $\rho = 0.9995$, 0.995, 0.9853, 0.9535, and 0.8771 for $N = 25$, 49, and 121, respectively. Table 1 shows a comparison between the weighted-difference variance and the system noise variance for these values of image correlation coefficients. Again, the Gaussian approximation agrees with the data better as N increases. It is apparent from this figure that we have good-to-reasonable agreement between
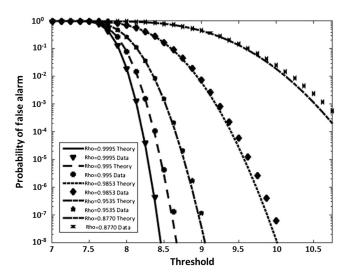

Fig. 9 Comparison of computer simulation results with probability of false alarm, Eq. (52), for $N = 49$ and $\rho = 0.9995$, 0.995, 0.9853, 0.9535, and 0.8771.
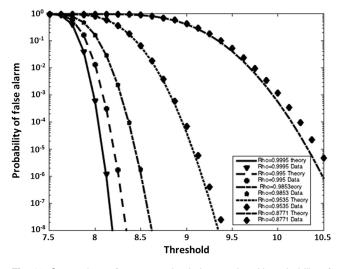

Fig. 10 Comparison of computer simulation results with probability of false alarm, Eq. (52), for $N = 121$ and $\rho = 0.9995$, 0.995, 0.9853, 0.9535, and 0.8771.

theory and simulation for image correlation coefficients of $\rho = 0.9995$, 0.995, and 0.9853. Referring to Table 1, this means that the assumption appears good for weighted-difference variances on the order of the differenced system noise variance level. The comparison for $\rho = 0.9535$ appears to be in good agreement for false alarm probabilities less than 10^{-3} but degrades as the false alarm probability goes to 10^{-4} and below and N is lower. Here, the weighted variance is over five (5) times the differenced system noise variance. For $\rho = 0.8771$, we find good agreement above the 50% level, but the comparison becomes poor for low false alarm probabilities and smaller values of N. This is not too surprising since the weighted variance is almost 14 times the differenced system noise variance. In both of these latter cases, our theory acts as a lower bound for the false alarm probability. Let us now look at the detection probability.

Figure 11 gives a comparison of the computer simulation results and the probability of detection using Eq. (59) as a function of the threshold for $\rho = 0.9995$, 0.995, 0.9853, 0.9535, and 0.8771 for $N = 121$. Similar plots are found for $N = 15$ and 49. In all cases, the comparison is good for all values of image correlation. This is not too surprising since we are always interested only in detection probabilities above a few percent levels where the noise floor under hypothesis 1 comprises the Gaussian system noise.

Table 1 Comparison of weighted-difference and differenced system noise variances for various image correlation coefficients.

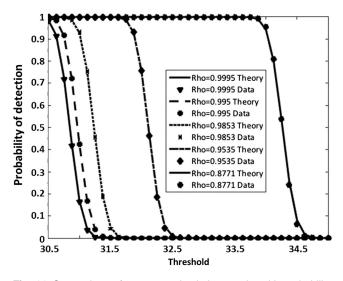| Image correlation coefficient	Weighted-difference variance	Differenced system noise variance
0.9995	0.001499625	0.025
0.995	0.0149625	0.025
0.9853	0.043775865	0.025
0.9535	0.136256625	0.025
0.8771	0.346043385	0.025

Fig. 11 Comparison of computer simulation results with probability of detection, Eq. (59), for $N = 121$ and $\rho = 0.9995$, 0.995, 0.9853, 0.9535, and 0.8771.

Our conclusion from the above is that this hypothesis test is good for those dual-band spectral image correlations where the resulting weighted difference variance is on the order of, or lower than, the differenced system noise variance. The correlation between images is still high but is not necessarily required to be above 0.9. This suggests that the test statistic is more robust than the approximation suggests, but it should not be expected to detect targets well when the correlation coefficient is low.

6 Application of Theory to Real Data

In this section, we will apply our theory to the TIMS dataset used by other LRT researchers, recognizing that we will be working with data containing coarsely resolved targets and no system noise. Our intent is to illustrate the theory's performance under nonoptimal conditions.

The six-band thermal infrared multispectral scanner (TIMS) data have been used by many researchers to validate

their additive-noise target detection algorithms over the years.[36,17] TIMS is an airborne sensor that covers six thermal infrared spectral bands with center wavelengths of 8.35, 8.74, 9.12, 9.83, 10.69, and 11.6 μm. Because of its design, the TIMS sensor does not have system noise. The TIMS dataset that will be used here is from a 1985 night experiment sensing terrain on the outskirts of Adelaide, Australia. These recorded data were 256×256 images of rural terrain covering several main roads, narrow secondary roads, and some structures. Pixel resolution was a nominal 8 m for this data run. Hallenborg et al. reported that there was a high band-to-band correlation among the various images in this dataset, which they expected for graybody radiation from natural terrain.[17]

Figures 12(a) and 12(b) show sample images from the TIMS channel 1 (8.35 μm) and channel 2 (8.74 μm) datasets, respectively. Qualitatively, both images look the same as expected. Figures 13(a) and 13(b) show the PDF histograms for the channel 1 and 2 images, respectively. Clearly, Figs. 12(a) and 12(b) show that sample images from the histograms look Gaussian-like, but they also look slightly different, and their tails are more populated than expected in a Gaussian distribution. Fortunately, the images are highly correlated. Figure 14 shows a scatterplot of these two images, illustrating good correlation between the two datasets. The correlation coefficient between these two sets of data is 0.9961. Similar PDFs, scatter plots, and correlations can be derived from analysis of images from channels 3 and 4 and channels 5 and 6. Following Xu et al.,[36] the images were high-pass filtered to remove the low-frequency spatial components using a 9×9 element blocking filter located at the origin in the Fourier plane of both images. Locations of the known targets set analyzed in this paper and in the aforementioned papers are shown in Fig. 15.[17]

As noted by Xu et al.[36] and Hallenborg et al.,[17] there is a large number of high-intensity points besides the chosen target set. These unresolved points can be traced to unresolved buildings and roads at the test site, which are clearly seen in Fig. 15. This figure depicts all pixel intensities greater than three standard deviations of the difference image of channels
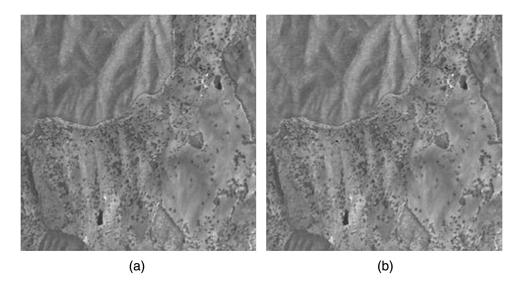

(a)

(b)

Fig. 12 (a) Adelaide TIMS channel 1 (256×256) image and (b) Adelaide TIMS channel 2 (256×256) image.
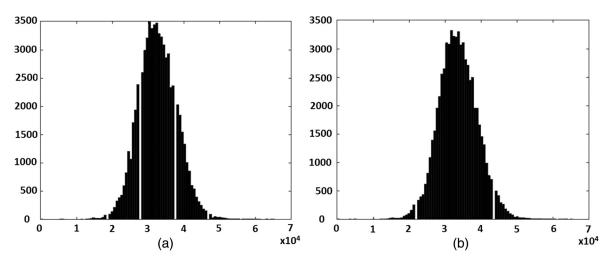
Fig. 13 (a) Histogram of Adelaide TIMS channel 1 image and (b) histogram of Adelaide TIMS channel 2.
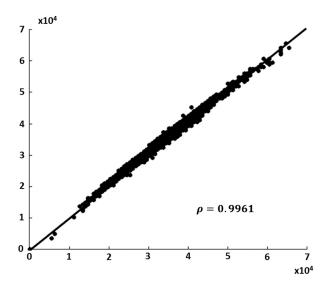

Fig. 14 Scatter plot of Adelaide TIMS channel 1 and Adelaide TIMS channel 2 intensity data.
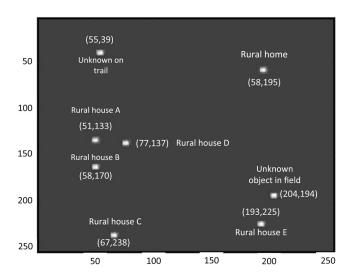

Fig. 15 Locations of the selected targets in the Adelaide TIMS images.

1 and 2 (the total number of pixels is 214). These residual structures essentially create a fixed pattern in all the TIMS imagery that create false detections when processed with anyone's LRT; that is, they resemble many of the selected targets identified in Fig. 15.

Let us now look at the CFAR performance of our detector against three sets of TIMs image pairs, channels 1 and 2, channels 3 and 4, and channels 5 and 6. In the previously cited works, Xu et al.[36] and Hallenborg et al.[17] used a spatial processing vector s created out of an 11×11 spatial processing window ($N = 121$) chosen for "reasonable detection loss" and "adaptability."[36] The center of the 11×11 window contains a 5×5 target shape distribution extracted from the image pixel area centered at (51,134), the location of rural house A. The additional pixels in this 5×5 profile contain intensities generated by terrain adjacent to the house. The additional pixels outside the shape profile, but within the 11×11 window, were set to zero. In this analysis, we will only use the exact number of pixels that comprise a selected target; specifically, we will use the three pixel contrasts containing the rural house A, which are located at (51, 133), (52,133), and (51,134), respectively, in all the images. One can call the target quasiresolved, which is not the theory's basic assumption. That said, the results below suggest that the theory may be useful in that situation as well. In addition, in all the original spectral images, rural house A essentially has intensity values close to those of the clutter levels and does not stand out, that is, it is a low-contrast target. The parameters needed in the test statistic are computed using the entire image; the final test statistic output parameters were derived from a smaller portion of the image away from the three-sigma points, namely, in an area defined by points $(x, y) = (1,1)$ to $(x, y) = (1,51)$ to $(x, y) = (100,51)$ to $(x, y) = (100,1)$.

Figure 17 shows all the detected points from processing channel 1 and 2 imagery using Eq. (41) and a CFAR level of 10^{-14}. The CFAR threshold was derived from Eq. (47). Of the eight possible targets shown in Fig. 15, the statistical test was only able to detect four of them, which included rural house A, our selected target. The rest of the points in this image are false detections. Comparing this figure to Fig. 16, the test was able to eliminate a large number of the possible false detection points, but not to the level the previous

Fig. 16 False target map comprised unresolved buildings and roads in Adelaide TIM imagery.

Fig. 18 Detections from processing channel 3 and 4 imagery using Eq. (41) and CFAR level of 10^{-14}.

researchers did. They detected seven potential targets, of which five were "true detections of similar structures when compared to ordinary satellite imagery."[17] That is a 71% success rate. Figure 17 shows many more, many of them clumped together. However, given the large difference between the sizes of the processing window, this result is not too bad.

Figure 18 depicts all the detected points from processing channel 3 and 5 imagery at a CFAR level of 10^{-14}. Of the eight possible targets, the statistical test was only able to detect three of them, again including rural house A. However, there is a large number of false target detections. Obviously, channels 3 and 4 were not a good choice for discriminating the real target from the residual building and road clutter.

Figure 19 shows all the detected points from processing channel 5 and 6 images at a CFAR level of 10^{-14}. Of the eight possible targets, the statistical test detected four, which
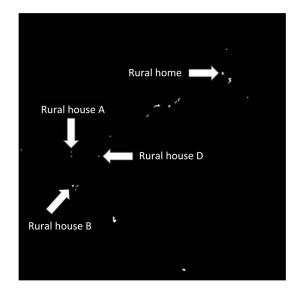
again included rural house A. Comparing this figure to Fig. 16, the test was able to eliminate most of the possible false detections, showing results more on the line that Xu et al.[36] and Hallenborg et al.[17] for channel 1 and 2 processing with their algorithms. This suggests that with the right selection of targets and two associated spectral bands, the test could provide good target detectability and false alarm rejection.

Table 2 compares the measured weighted-difference and test statistic variances derived from the test statistic processing of the three TIMS channel sets. Clearly, the correlation coefficient is very high between the channel sets, as noted earlier. The weighted-difference standard deviations agree very well, providing clutter reduction similar to that in side-lobe canceler applications. Unfortunately, the test statistic standard deviations are reasonably close but not in agreement as in the theoretical calculation. The author believes this is because the standard deviation approximation

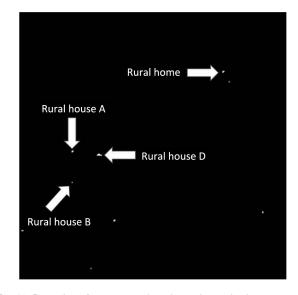**Fig. 17** Detections from processing channel 1 and 2 imagery using Eq. (41) and CFAR level of 10^{-14}.

Fig. 19 Detections from processing channel 5 and 6 imagery using Eq. (41) and CFAR level of 10^{-14}.

Table 2 Comparison of weighted-difference and test statistic variances for the three processed thermal infrared multispectral scanner (TIMS) channel sets.

TIMS images used	Image correlation coefficient	Weight difference standard deviation calculation	Weight difference standard deviation measurement	Test statistic standard deviation calculation	Test statistic standard deviation measurement
Channels 1 and 2	0.9958	429.506	429.51	7.25×10^6	7.18×10^6
Channels 3 and 4	0.9958	429.51	429.51	2.05×10^6	1.78×10^6
Channels 5 and 6	0.9874	671.33	671.33	9.75×10^5	8.95×10^6

Table 3 Comparison of original image and weighted-difference test statistics contrast-to-noise ratios (CNRs) and the effective CNR improvement obtained.

TIMS images used	Pixel (133, 51) original contrast-squared	Original image clutter variance	Original image CNR (dB)	Test statistic pixel (133, 51) measurement	Weighted-difference variance measurement	Test statistical CNR measurement (dB)	CNR improvement (dB)
Channels 1 and 2	7.06×10^6	2.20×10^{-7}	-4.95×10^{-1}	8.36×10^6	1.84×10^5	16.56	21.51
Channels 3 and 4	1.96×10^7	2.31×10^7	-7.11×10^{-1}	1.15×10^7	1.84×10^5	17.94	18.66
Channels 5 and 6	4.30×10^6	1.80×10^7	-6.22×10^{-1}	1.55×10^7	4.51×10^5	15.37	21.58

for the noncentral chi-squared PDF usually requires a large N to achieve a Gaussian approximation under the central limit theorem. In addition, the presence of the fixed residual pattern and lack of system noise probably contribute to the differences as well. Table 3 shows the improvement by the test statistic processing relative to the original image, which is above 18 dB in all cases. This table suggests a significant improvement in target detectability from the proposed test statistic. Although the data did not meet all the theory's assumptions, the demonstrated performance in the above figures and tables is encouraging and offers a potentially important tool for processing dual-channel, resolved target imagery with reasonable complexity and effectiveness. More validation of this test statistic is certainly warranted if appropriate datasets can be found.

7 Summary

This paper developed a log-likelihood ratio test statistic for resolved target detection in dual-band imagery because previous work indicates that most of the processing gains come from processing just two bands. Simple, closed-form equations for its closed-form probabilities of false alarm and detection are provided. Computer simulation results validated the theory. A CFAR version of the theory is applied to real, available multiband data with quasiresolved target sets and fixed bandwidth noise. The results show very reasonable performance in target detectability using three sets of correlated dual-band images. Finally, the paper showed that the resolved target detection problem depends on the weighted difference between the dual-band target contrasts. The theoretical development reaffirms that the SNR/CNR is approximately that weighted difference squared, divided by the normalized total image noise variance.

References

1. I. S. Reed, L. B. Stotts, and R. M. Gagliardi, "Optical moving target detection with three-dimensional matched filtering," *IEEE Trans. Aerosp. Electron. Syst.* **24**(4), 327 (1988).
2. L. B. Stotts, "Moving target indication techniques for optical image sequences," PhD Thesis, Univ. of California (1988).
3. I. S. Reed, L. B. Stotts, and R. M. Gagliardi, "A recursive moving target indication algorithm," *IEEE Trans. Aerosp. Electron. Syst.* **26**(3), 434 (1990).
4. F. C. Robey et al., "A CFAR adaptive matched filter detector," *IEEE Trans. Aerosp. Electron. Syst.* **28**(1), 208–216 (1992).
5. T. Soni, J. R. Zeidler, and W. H. Ku, "Performance evaluation of 2-dimensional adaptive prediction filters for detection of small objects in image data," *IEEE Trans. Image Process.* **2**(3), 327–340 (1993).
6. L. E. Hoff et al., "Generalized weighted spectral difference algorithm for weak target detection in multiband imagery," *Proc. SPIE* **2561**, 12, 141–152 (1995).
7. L. E. Hoff et al., "Enhanced classification performance from multiband infrared imagery," in *Proc. Twenty-Ninth Asilomar Conf. on Signals, Systems & Computers Proceedings*, Vol. 2, pp. 837–841 (1995).
8. X. Yu et al., "Automatic target detection and recognition in multi-band imagery: a unified ML detection and estimation approach," *IEEE Trans. Image Process.* **6**(1), 143–156 (1997).
9. A. Stocker and A. Schaum, "Spectrally-selective target detection," in *Proc. Int. Symp. on Spectral Sensing Research*, B. A. Mandel, Ed., p. 23l, Int. Society of Photogrammetry and Remote Sensing, San Diego, California (1997).
10. D. Manolakis et al., "Is there a best hyperspectral detection algorithm?," *Proc SPIE* **7334**, 733402 (2009).
11. J. W. Boardman, "Analysis understanding and visualization of hyperspectral data as convex sets in n-space," *Proc. SPIE* **2480**, 14–22 (1995).
12. J. M. Grossmann et al., "Hyperspectral analysis and target detection system for the adaptive spectral reconnaissance program (ASRP)," *Proc. SPIE* **3372**, 2–13 (1998).
13. M. E. Winter, "Fast autonomous spectral endmember determination in hyperspectral data," in *Proc. Thirteenth Int. Conf. on Applied Geologic Remote Sensing*, Vol. 2, pp. 337–344 (1999).
14. M. E. Winter, "N-FINDR: an algorithm for fast autonomous spectral end-member determination in hyperspectral data," *Proc. SPIE* **3753**, 266–275 (1999).
15. S. G. Beaven, D. Stein, and L. E. Hoff, "Comparison of Gaussian mixture and linear mixture models for classification of hyperspectral data," *IGARSS* 24–28 (2000).
16. L. E. Hoff and E. M. Winter, "Stochastic target detection," in *Proc. MSSS on CC&D*, Veridian ERIM International (2001).

17. E. Hallenborg, D. L. Buck, and E. Daly, "Evaluation of automated algorithms for small target detection and non-natural terrain characterization using remote multi-band imagery," *Proc. SPIE* **8137**, 813711 (2011).
18. A. P. Schaum and B. J. Daniel, "Continuum fusion methods of spectral detection," *Opt. Eng.* **51**, 111718 (2012).
19. A. Schaum, "Enough with the additive target model," *Proc. SPIE* **9088**, 90880C (2014).
20. A. P. Schaum, "Continuum fusion solutions for replacement target models in electro-optic detection," *Appl. Opt.* **53**(13), C25–C31 (2014).
21. L. B. Stotts and L. E. Hoff, "Statistical detection of resolved targets in background clutter using optical/infrared imagery," *Appl. Opt.* **53**(22), 5042–5052 (2014).
22. A. D. Stocker et al., "Analysis of infrared multispectral target/background field measurements," *Proc. SPIE* **2235**, 148–161 (1994).
23. C. R. Schwartz, J. N. Cederquist, and T. J. Rogne, "Comparison of modeled to measured infrared multispectral target/background signatures," *Proc. SPIE* **2235**, 162–184 (1994).
24. J. N. Cederquist and C. R. Schwartz, "Performance tradeoffs of infrared spectral imagers: II," *Proc. SPIE* **3438**, 114–122 (1998).
25. J. N. Cederquist et al., "Performance trade-offs of infrared spectral imagers," *Proc. SPIE* **3118**, 23–27 (1997).
26. P. Marzoulis, "Spectral and spatial uniformity in pushbroom imaging spectrometers," *Proc. SPIE* **3753**, 133–141 (1999).
27. D. W. J. Stein et al., "Anomaly detection from hyperspectral imagery," *IEEE Signal Process. Mag.* **19**, 58–69 (2002).
28. D. G. Manolakis et al., "Apparent superiority of sophisticated detection algorithms in test conditions does not necessarily imply the same in real-world hyperspectral imaging applications," *SPIE Newsroom* (2009).
29. B. Zhang et al., "Real-time target detection in hyperspectral images based on spatial-spectral information extraction," *EURASIP J. Adv. Signal Process.* **2012**, 142 (2012).
30. Y. Cohen et al., "Evaluating subpixel target detection algorithms in hyperspectral imagery," *J. Electr. Comp. Eng.* **2012**, 15 (2012).
31. K. Fukunaga, Ed., *Introduction to Statistical Pattern Recognition*, 2nd ed., Academic Press, New York (1990).
32. C. W. Helstrom and J. A. Ritcey, "Evaluating radar detection probabilities by steepest descent integration," *IEEE Trans. Aerosp. Electr. Syst.* **AES-20**, 624–634 (1984).
33. S. W. Smith, *The Scientist and Engineer's Guide to Digital Signal Processing*, pp. 423–450, California Technical Publishing, San Diego, California (1997).
34. I. S. Reed and X. Yu, "Adaptive multiple-band CFAR detection of an optical pattern with unknown spectral distribution," *IEEE Trans. Acoust. Speech Signal Process.* **38**, 1760–1770 (1990).
35. L. E. Hoff, J. R. Evans, and L. E. Bunney, "Detection of targets in terrain clutter by using multi-spectral infrared image processing," Naval Ocean Systems Center (NOSC), Report TD 1404 (1990).
36. X. Yu, I. S. Reed, and A. D. Stocker, "Comparative performance analysis of adaptive multispectral detectors," *IEEE Trans. Signal Process.* **41**, 2639–2656 (1993).
37. A. D. Stocker, I. S. Reed, and X. Yu, "Multidimensional signal processing for electro-optic target detection," *Proc. SPIE* **1305**, 218–231 (1990).
38. E. Winter and M. J. Schlangen, "Detection of extended targets using multi-spectral infrared," *Proc. SPIE* **1954**, 173–180 (1993).
39. L. B. Stotts et al., "Clutter rejection using multispectral processing," *Proc. SPIE* **1305**, 2–10 (1990).
40. M. I. Skolnik, *Introduction to Radar Systems*, 2nd ed., pp. 333, McGraw-Hill Book Company, New York (1980).
41. E. L. Oberstar, "Advanced signal processing: sidelobe canceller beam former," www.superkits.net/whitepapers/SidelobeCanceller.pdf (2001).

Larry B. Stotts is a resident consultant at Science and Technology Associates. He holds a BA degree in applied physics and information sciences and a PhD in electrical engineering (communications systems), both from the University of California at San Diego. He is the author of more than 100 journal articles, conference papers, and technical reports, and a coauthor of two books and two book chapters. His research interests include RF and laser communications and networking, optical propagation in random and particulate media, image processing, and E/O system design. He is a fellow of SPIE and IEEE and a senior member of the Optical Society of America.